



# Earth's radiative imbalance from the Last Glacial Maximum to the present

Daniel Baggenstos<sup>a,b,1</sup>, Marcel Häberli<sup>a,b</sup>, Jochen Schmitt<sup>a,b</sup>, Sarah A. Shackleton<sup>c</sup>, Benjamin Birner<sup>c</sup>, Jeffrey P. Severinghaus<sup>c</sup>, Thomas Kellerhals<sup>a,b</sup>, and Hubertus Fischer<sup>a,b</sup>

<sup>a</sup>Climate and Environmental Physics, Physics Institute, University of Bern, 3012 Bern, Switzerland; <sup>b</sup>Oeschger Centre for Climate Change Research, University of Bern, 3012 Bern, Switzerland; and <sup>c</sup>Scripps Institution of Oceanography, University of California San Diego, La Jolla, CA 92093

Edited by Mark H. Thiemens, University of California San Diego, La Jolla, CA, and approved June 4, 2019 (received for review April 1, 2019)

The energy imbalance at the top of the atmosphere determines the temporal evolution of the global climate, and vice versa changes in the climate system can alter the planetary energy fluxes. This interplay is fundamental to our understanding of Earth's heat budget and the climate system. However, even today, the direct measurement of global radiative fluxes is difficult, such that most assessments are based on changes in the total energy content of the climate system. We apply the same approach to estimate the long-term evolution of Earth's radiative imbalance in the past. New measurements of noble gas-derived mean ocean temperature from the European Project for Ice Coring in Antarctica Dome C ice core covering the last 40,000 y, combined with recent results from the West Antarctic Ice Sheet Divide ice core and the sea-level record, allow us to quantitatively reconstruct the history of the climate system energy budget. The temporal derivative of this quantity must be equal to the planetary radiative imbalance. During the deglaciation, a positive imbalance of typically  $+0.2 \text{ W}\cdot\text{m}^{-2}$  is maintained for  $\sim 10,000 \text{ y}$ , however, with two distinct peaks that reach up to  $0.4 \text{ W}\cdot\text{m}^{-2}$  during times of substantially reduced Atlantic Meridional Overturning Circulation. We conclude that these peaks are related to net changes in ocean heat uptake, likely due to rapid changes in North Atlantic deep-water formation and their impact on the global radiative balance, while changes in cloud coverage, albeit uncertain, may also factor into the picture.

palaeoclimate | deglaciation | noble gases | energy budget | ice cores

Global climate change arises from a planetary radiative imbalance (PRI) at the top of the atmosphere. The imbalance amounts to the difference between solar energy absorbed by Earth and energy the planet radiates back into space. It is therefore a fundamental climate parameter that describes the state of the planetary energy balance at all times (1). For the current global warming period—specifically, the decade from 2001 to 2010—the imbalance has been estimated to  $0.50 \pm 0.43 \text{ W}\cdot\text{m}^{-2}$  using carefully calibrated space-borne radiometers (2) as well as continuous measurements of the ocean heat content (OHC; refs. 3–7) down to an ocean depth of 2,000 m. The globally integrated signal of PRI from satellite measurements is difficult to assess even today, due to the large temporal and spatial variability of the underlying radiative fluxes (8–10).

Additional information on the potential range of the planetary radiation imbalance can be gained from past climate changes. These include the  $\sim 3.5\text{-K}$  global warming over the last deglaciation (11), as well as times of rapid climate change related to variations in the strength of the Atlantic Meridional Overturning Circulation (AMOC), which locally exhibit warming rates higher than the current anthropogenic warming (12) and may even affect the global radiative fluxes (13). However, little is known about the energy imbalance in the past. Logical inference dictates that the PRI was positive during periods of global mean warming, such as the deglaciation, and negative during global cooling phases. Up to now, no attempt has been made to quantify PRI (let

alone its temporal evolution) for the most recent deglaciation (14) from the Last Glacial Maximum (LGM;  $\sim 21 \text{ ka}$ ) to the early Holocene ( $\sim 10 \text{ ka}$ ), due to a lack of direct proxies of past global radiative fluxes. Thus, the indirect method of determining the total system energy change and inferring the necessary flux imbalance is the only way to reconstruct the paleoradiation budget at the top of the atmosphere. Due to energy conservation, the net radiation flux across the upper atmospheric boundary at any point in time must exactly equal the rate of change of the sum of the heat content of all components of the climate system (8). The energy available due to geothermal heating (typically  $<0.1 \text{ W}\cdot\text{m}^{-2}$ ) is small in comparison with the solar radiation flux. Moreover, its temporal changes are so small that they can be safely neglected in energy-balance studies over the last 20,000 y (5, 15, 16).

The ocean is the dominant energy reservoir in the climate system due to its high heat capacity and efficient transport of heat into the ocean interior by advection and diffusion. More than 90% of the excess heat during the ongoing global warming is taken up by the ocean (16, 17). With improvements in the method of noble gas mean ocean thermometry (18, 19), it has now become possible to quantify changes of the oceanic heat reservoir in the past at high temporal resolution and improved precision (20). On glacial/interglacial time scales, a second heat reservoir is of comparable importance as the OHC—namely, the latent heat associated with the waxing and waning of the continental ice sheets. The contribution of this part of the climate system to the total energy content is directly proportional to the change in continental ice mass. Continental ice loss, in turn,

## Significance

Earth's radiative imbalance determines whether energy is flowing into or out of the ocean-atmosphere system. The present, anthropogenic, positive imbalance drives global warming. This study reconstructs the radiative imbalance for the last deglaciation,  $\sim 20,000$  to  $10,000 \text{ y}$  ago. During the deglaciation, a positive imbalance was maintained for several thousand years, which brought the climate system from the last ice age into the Holocene warm period. We show that the imbalance varied significantly during this time, possibly due to changes in ocean circulation that affect the radiative energy fluxes, highlighting the importance of internal variability in Earth's energy budget.

Author contributions: J.S., T.K., and H.F. designed research; D.B. and M.H. performed measurements; D.B., M.H., J.S., S.A.S., B.B., J.P.S., T.K., and H.F. analyzed data; and D.B. wrote the paper with input from all authors.

The authors declare no conflict of interest.

This article is a PNAS Direct Submission.

Published under the PNAS license.

<sup>1</sup>To whom correspondence may be addressed. Email: baggenstos@climate.unibe.ch.

This article contains supporting information online at [www.pnas.org/lookup/suppl/doi:10.1073/pnas.1905447116/-DCSupplemental](http://www.pnas.org/lookup/suppl/doi:10.1073/pnas.1905447116/-DCSupplemental).

Published online July 8, 2019.

is reflected by a change in ocean mass and volume, and thus global mean sea level (GMSL), which has been reconstructed for the last deglaciation with sufficient accuracy (21, 22). All other terms in the global energy budget are at least an order of magnitude smaller (*SI Appendix*). Thus, the sum of OHC change and GMSL-derived latent heat storage of land ice is a good first-order representation of the total energy change in the climate system, the temporal slope of which can be used to derive PRI in the past.

## Results

**OHC Record.** To reconstruct the OHC evolution during the deglaciation, we used the recent mean ocean temperature (MOT) assessment from the West Antarctic Ice Sheet Divide (WD) ice core (20) alongside a new dataset from the European Project for Ice Coring in Antarctica (EPICA) Dome C (EDC) ice core presented here (Fig. 1). Both records are based on noble gas thermometry, which uses the ratio of heavy noble gases in the paleo atmosphere to infer past MOTs via the gas-specific, temperature-dependent solubilities of atmospheric gases in the ocean (*Materials and Methods*). The paleo atmospheric signal should be identical at WD and EDC, but site-specific firn fractionation corrections and storage effects could cause differences between the two records. The generally good agreement of WD and EDC OHC proves the soundness of the principles underlying noble gas mean ocean thermometry, even though the two ice cores represent two end members of site conditions for Antarctic drill sites. The ocean warming from the LGM to the early Holocene is achieved in two stages, interrupted by a period of

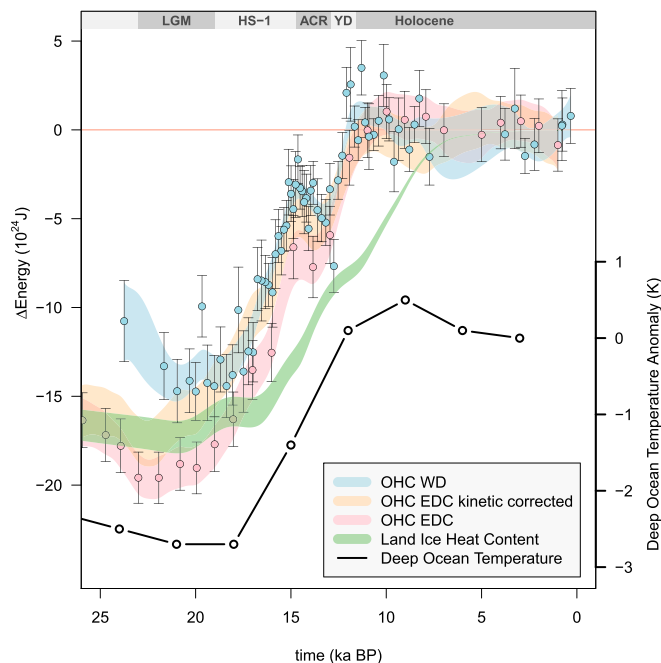


**Fig. 1.** OHC change relative to the late Holocene average, derived from WD (blue) and EDC (pink and orange) ice core noble gas records, including a  $1\text{-}\sigma$  confidence band based on Monte Carlo smoothing splines with 2,500-y cutoff period. The orange band shows the EDC OHC record if a correction for differential kinetic fractionation (*SI Appendix*) is applied. The green line shows the heat anomaly associated with the continental glaciation derived from the sea-level record (21), also splined with a 2,500-y cutoff period. In black, the deep ocean temperature reconstruction from ref. 31 is shown. The gray bar on top indicates specific climate periods discussed in the main text: Last Glacial Maximum (LGM), Heinrich Stadial 1 (HS-1), Antarctic Cold Reversal (ACR), Younger Dryas (YD), and the Holocene.

slight cooling from 14.6 to 12.8 ka, coinciding with the Antarctic Cold Reversal (ACR) observed in Antarctic ice core records (23) and the Bølling–Allerød warm stage in the North Atlantic (24).

After the OHC maximum at  $\sim 10$  ka, there is little change or, if at all, a slight cooling up to historic times. There is an ongoing discussion about surface-temperature trends during the Holocene warm period, with proxy reconstructions showing warmer temperatures from 10 to 6 ka followed by a clear (mostly Northern Hemisphere high latitude) cooling through the middle to late Holocene, while model simulations estimate a gradual warming (25, 26). The most likely culprits for this disparity are seasonal (summer) biases on the proxy data side, as well as insufficient sensitivity (e.g., on sea ice) and additional feedbacks on the model side (27). During times of relatively stable ocean circulation, such as the Holocene, MOT/OHC should be mainly coupled to high-latitude sea-surface temperatures (SSTs), likely with a bias toward winter temperature since deep-water formation is most sensitive to winter conditions (28). Our MOT data do not show a pronounced Holocene cooling found in many high-latitude proxies, but, in contrast to SST in models, MOT reaches Holocene values much earlier ( $\sim 11$  ka) and remains flat throughout the Holocene. Our data thus point to the high-latitude early Holocene warmth in ref. 25 not being restricted to the summer season.

The main systematic difference between the WD and EDC records in Fig. 1 is the magnitude of the glacial/interglacial change, with  $19.0 \times 10^{24}$  J for EDC and  $14.0 \times 10^{24}$  J for WD (equivalent to 3.5- and 2.6-K temperature changes, calculated at  $20 \pm 1$  ka for the LGM and  $10 \pm 1$  ka for the early Holocene). Both are consistent with estimates of deep-ocean deglacial temperature change (29–31), keeping in mind that the noble gas thermometry results encompass the integrated global ocean, whereas sediment-based reconstructions are local by nature. The discrepancy between EDC and WD can likely be attributed to an imperfect correction for gas-fractionating processes in the firn column by using high-precision noble gas isotope analyses. The reconstructed glacial/interglacial OHC difference is sensitive to systematic uncertainties in our understanding of firn gas-transport processes. For example, including a correction term for differential kinetic fractionation (32) reduces the EDC glacial/interglacial MOT difference to 2.7 K (*SI Appendix*). Accordingly, based on our current knowledge of the firn column at EDC and WD, we cannot determine the absolute net glacial/interglacial heat uptake by the ocean to better than 20%. The amplitude of our derived PRI estimate scales with this glacial/interglacial net energy uptake and is, therefore, also subject to an uncertainty of 20%. However, the relative temporal changes in the imbalance are largely independent of the absolute level. Our conclusions on ocean heat-uptake anomalies during the deglaciation are therefore not affected by the use of a specific MOT record.

To avoid erroneous variability in the PRI due to the measurement noise in the MOT reconstruction, we used a low-pass filtered version of each OHC record (spline approximation with 2,500-y cutoff period). Thus, we reconstructed only the average PRI that is typical for these long time scales, whereas higher-frequency variation in PRI could be significantly larger.

**Melting Ice Sheets.** Fig. 1 also shows the energy required to melt land ice equivalent in volume to 130 m of GMSL rise. This ice-sheet contribution to the energy budget (latent heat of melting; LHM) is assessed with the sea level record of Lambeck et al. (ref. 21; *Materials and Methods*). As we are interested in the millennial averaged PRI, we again used a spline approximation of the sea-level record with a cutoff period of 2,500 y. This also implies that short-term events such as Meltwater Pulse 1A at 14.6 ka are not resolved in this record. Curiously, the total amount of heat taken up by the ocean over the entire deglacial transition is very similar

to the total LHM; however, the oceanic component reacts faster and reaches a new equilibrium more quickly than the land-ice contribution. The latter begins to increase slightly later and stabilizes only at 7 ka, once approximately modern ice volume has been reached.

**PRI.** The reconstructed PRI based on OHC and LHM (Fig. 2 a and b) exhibits two peaks at 15.5 and 12.5 ka, separated by a period of more balanced radiative fluxes during the ACR. The reconstructed contribution of heat exchange with the global ocean points to no heat uptake or even a slight heat release during the ACR, while the latent heat sink by ice-sheet melting was at a maximum (*SI Appendix, Fig. S1*). Further, the two peaks in PRI during Heinrich Stadial 1 (HS-1) and the Younger Dryas (YD) are linked to strong increases in OHC. The magnitude of the peaks is not well constrained since it depends on the amount

of smoothing applied to the raw data (*SI Appendix, Fig. S2*). During the LGM and Holocene, the net radiative flux is close to zero, as expected from the relative stability of these climate periods. WD- and EDC-derived PRI generally agree well within their uncertainties. The most notable difference between the PRI reconstruction using EDC and WD is a sharper YD peak in WD. However, recent work by Shackleton et al. (33) suggests that the OHC increase during the YD based on WD may be anomalously high, which would reconcile the two records.

## Discussion

**Long-Term Changes in Global Radiative Forcing over the Deglaciation.** The PRI is a function of both the radiative forcing due to a (external) perturbation of the net irradiance (e.g., through a change in the concentration of greenhouse gases in the atmosphere) and the surface-temperature response to such forcing (34). The energy imbalance reflects the part of the forcing to which the temperature hasn't had time to adjust, due to the long reequilibration time scales of many components of Earth system (6). Following Murphy et al. (5), the top-of-atmosphere (TOA) energy balance can be written as

$$PRI = F - \alpha \Delta T, \quad [1]$$

with  $PRI$  as the net energy flow toward Earth,  $F$  the radiative forcing, and  $\alpha \Delta T$  the change in outgoing radiation caused by a change  $\Delta T$  in the planetary surface temperature.  $\alpha$  is a linearization parameter that best describes the time-scale-dependent energy imbalance (5), and  $1/\alpha$  should approach Earth-system sensitivity after a sufficiently long equilibration time. The linearization in Eq. 1 is justified, as Earth's outgoing longwave radiation does not follow classical Stefan-Boltzmann theory, but increases linearly with surface temperature (35) due to the water-vapor feedback (36). A hypothetical jump in radiative forcing  $F$  by  $1 \text{ W}\cdot\text{m}^{-2}$  will lead to global surface warming that reduces the PRI surplus until a balanced budget is reached again (3). This reequilibration process per se is faster than our records are able to resolve (37). To keep the budget unbalanced for several thousand years, as seen in Fig. 2, continuously increasing forcings are needed, such as positive feedbacks of the biogeochemical cycles to the initial warming or long-term changes in the planetary albedo. In line, a positive global radiation anomaly is predicted for the entire deglaciation, but the observed pattern of two PRI peaks separated by a period of lower disequilibrium is unexpected and needs to be explained.

Several individual contributions to the radiative forcing on glacial/interglacial time scales have been estimated by using climate models (Fig. 2 e–i; ref. 38): The changes in incoming shortwave radiation due to continuously varying orbital parameters are well known, as the equations governing planetary orbits can be solved with high accuracy for the Pleistocene (39). While local or seasonal changes to the radiation budget are substantial on these time scales, the annual and global average insolation received by Earth remains essentially unchanged. The capacity of greenhouse gases in the atmosphere to reduce outgoing longwave radiation by trapping infrared radiation has long been understood (40). Concentrations of  $\text{CO}_2$ ,  $\text{CH}_4$ , and  $\text{N}_2\text{O}$  all increased from a minimum in the LGM to a maximum in the Holocene as a result of changes in the biogeochemical and physical processes that control them (41–44), comprising a total  $2.9 \text{ W}\cdot\text{m}^{-2}$  increase in the TOA radiative balance (45). Planetary surface reflectivity has a considerable influence on the shortwave radiative fluxes. In the LGM, boreal forests were replaced by high-albedo continental ice sheets, which represents the largest factor contributing to albedo changes (38). In addition, other elements, such as changes in seasonal snow cover, sea ice coverage, global vegetation, land area due to sea level lowering, and cloud cover added to the planetary albedo change. These

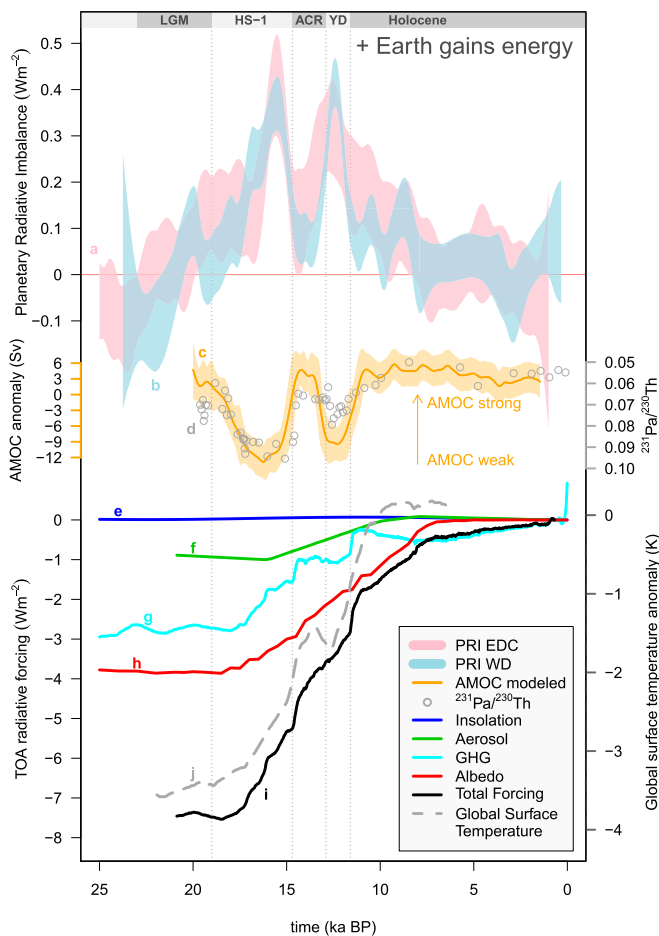


**Fig. 2.** Reconstructed PRI, overturning circulation, estimated forcings, and GST from the LGM to the present: PRI using the EDC (a) and WD (b) OHC records with  $1\text{-}\sigma$  confidence band. The enhanced uncertainty at the beginning and end of the PRI reconstructions are edge effects of the spline fitting. (c) Modeled AMOC strength from the LOVECLIM intermediate complexity climate model (52). (d) The protactinium/thorium record from a subtropical North Atlantic sediment core (51), a proxy for the meridional overturning with higher  $^{231}\text{Pa}/^{230}\text{Th}$  implying weakened circulation. (e) Global mean annual insolation forcing (69). (f) Global dust fluxes from ref. 48 scaled to  $1 \text{ W}\cdot\text{m}^{-2}$  in the LGM, which is an average of the surveyed literature on aerosol radiative forcing in the glacial (47). (g) Greenhouse gas (GHG) forcing from ref. 45. (h) Radiative forcing from albedo changes as estimated by ref. 46, scaled to the (70) ICE-6G ice sheet area. (i) Total forcing as the sum of e–h. (j) GST reconstruction (11). The gray bar on top indicates specific climate periods discussed in the main text.

are less certain and are not included in Fig. 2, but may be relevant for variability in the global radiative budget on top of these long-term changes (see below). The impacts of the LGM ice sheet and the implied changes in land–sea distribution on the radiative budget are assessed by Abe-Ouchi et al. (46) with 11 climate models of intermediate complexity, which yield an average radiative forcing of  $3.9 \text{ W}\cdot\text{m}^{-2}$  (spread  $2.7$  to  $5.2 \text{ W}\cdot\text{m}^{-2}$ ). The temporal evolution of this forcing from the LGM to the preindustrial era has not been studied in detail, but should to first-order scale with the amount of ice-covered land area. The final radiative forcing contribution considered here is due to changes in the atmospheric dust load. There is a broad consensus that the global dust cycle was more active in the LGM than today, but the radiative impact of the evolving dust load ranges from  $-2.0$  to  $+0.1 \text{ W}\cdot\text{m}^{-2}$  in various studies (47) because the dust shortwave radiative effect depends strongly on the size and type of the dust particles. Furthermore, the spatiotemporal evolution of the dust load during the deglaciation is poorly known, although there have been attempts to quantify it using models (48). Other aspects that could affect the TOA radiative fluxes, such as changes in cloud coverage or atmospheric chemistry, are highly uncertain (49), and thus cannot be included in this compilation.

**Additional Short-Term Changes in the Radiative Forcing.** Our PRI reconstruction over the transition shows typical values of  $+0.2 \text{ W}\cdot\text{m}^{-2}$ , implying that the warming is sustained due to slow positive feedbacks, which keep the system out of radiative equilibrium throughout the multimillennial climate changes during the glacial termination. This is to be expected, given the long equilibration times of the large continental ice sheets and the ocean. However, the described forcings and the latest reconstructed global surface temperature (GST) change (11) are not always consistent with the PRI as predicted by Eq. 1. In particular, the highest rate of change of the total forcing in Fig. 2 is found at the end of HS-1 and the YD. At the same time, the increase in GST is enhanced, whereas the radiative imbalance shows maxima during HS-1 and the YD. During the ACR, the total forcing shows a continuing increase, but GST is increasing less or even decreasing (11), which implies, according to Eq. 1, a large radiative imbalance, contrary to our reconstruction. The apparent decoupling of the record in radiative imbalance at the top of the atmosphere on the one hand and the forcings and GST on the other during these intervals indicates that there must be additional processes not yet considered to explain the discrepancies.

**Ocean Circulation.** The most likely candidate for such a process is the radiative impact of changes in the global ocean overturning circulation (13). Several models have shown that a reduction of the AMOC leads to an accumulation of heat in the ocean interior (13, 15, 50), while an AMOC recovery lowers OHC. In the Atlantic Ocean, heat diffusing into the interior at low latitudes is in constant competition with the southward advection of cold subsurface water from North Atlantic deep-water formation sites. Thus, a reduced AMOC leads to increased subsurface temperatures in the Atlantic and, consecutively, the interior ocean, and vice versa. From a planetary point of view, the energy to heat the ocean has to be provided via a TOA radiative imbalance. In this case, the radiative response is a result of the surface cooling centered in the North Atlantic region. During an AMOC reduction, as implied during HS-1 and the YD (51, 52), the decrease of outgoing longwave radiation from the locally cooler ocean surface is larger than the reduction of incoming shortwave radiation, due to higher surface albedo via increased sea-ice concentration, causing a net positive global radiation anomaly of  $\sim 0.5 \text{ W}\cdot\text{m}^{-2}$  in the models (13), very similar to the magnitude of the variability in our reconstruction. The opposite process is observed

in the models during an AMOC recovery. This implies that, during the ACR, the radiative response is dominated by the local North Atlantic warming, even though the GST decreases. Thus, the impacts of circulation changes during the deglaciation [characterized by a back-and-forth in overturning circulation strength (51) with a weak AMOC during HS-1 and the YD and a strong AMOC during the ACR] on the energy imbalance at the top of the atmosphere are consistent with our PRI results.

**Low-Level Clouds.** An additional effect leading to the reduction of PRI during the ACR could be a change due to the net cloud radiative forcing, in particular at low latitudes. With the recovery of the AMOC during the ACR, the Intertropical Convergence Zone (ITCZ) most likely migrated to a more northerly position (42, 53) following Earth's thermal equator. This rearrangement of the atmospheric circulation could affect the cloud regime in the subtropical subsidence regions. Low-level clouds have an especially strong negative effect on the energy balance because they reflect solar radiation efficiently, and yet their emission temperature is similar to that of the underlying ocean surface. Furthermore, the radiative energy fluxes in low latitudes are substantially larger than in the mid or high latitudes, allowing for a relatively small change in cloud distribution to have a large impact on Earth's energy balance.

Also of note is the timing of the PRI peak at 15.5 ka, which occurs in the latter part of HS-1, even though ocean-sediment proxies indicate that the overturning circulation in the North Atlantic was reduced throughout the entire Heinrich stadial. This discrepancy may be related to an extreme southern position of the ITCZ with a switch in the hydrologic cycle and expansion of sea ice in the north starting at 16.2 ka (refs. 42 and 54 and references therein).

## Conclusion

Our study presents an attempt to investigate past changes in OHC and land-ice volume in the framework of global radiative flux and energy considerations. Our PRI reconstruction suggests that internal variability in the climate system is critical to understanding the global energy fluxes on millennial time scales. In particular, as deep ocean circulation is expected to slow in the future (34), Earth may accelerate its rate of heat uptake. To further evaluate an AMOC influence on the radiative balance, it would be valuable to determine OHC changes across major Dansgaard–Oeschger events (12), which are thought to represent disruptions in the global overturning circulation (50, 55) but are unaffected by the long-term dynamics of a deglacial transition. A caveat to our analysis concerns the uncertainty in internal climate feedbacks. A better understanding of aerosol and cloud radiative effects as well as reconstruction of past aerosol loading and cloud cover are needed to make progress in closing Earth's radiation budget. In addition, continuing work on understanding firn gas processes are paramount to reduce the uncertainties in noble gas-based OHC reconstructions.

## Materials and Methods

**Ice Core Measurements.** A total of 39 ice samples spanning 40 ka BP to present in  $\sim 1,000$ -y resolution from the EDC ice core were analyzed at the University of Bern for elemental and isotopic composition of nitrogen, argon, krypton, and xenon. The gas extraction and processing followed broadly the method (1) of Bereiter et al. (19) with a few notable differences: Sample size was only  $\sim 600$  g; cryogenic trapping of the gases was achieved with a cryostat instead of liquid helium; no water bath was used in the overnight equilibration; and we were able to report xenon isotopic ratios at similar precision as for krypton. All gas data are presented with respect to the modern atmosphere, consisting of regular measurements of ambient air collected in Bern, Switzerland. The long-term reproducibility of the system (given as the SD of 28 measurements of "ambient air" over 10 mo) is shown in *SI Appendix, Table S2*. Interlaboratory comparisons of selected ice samples have shown excellent agreement between the Bern and San Diego laboratories. Of the 39 measurements, one was rejected due to a procedural

problem. The Antarctic Ice Core Chronology 2012 age scale was used for all EDC samples (56).

**Firn Fractionation Corrections.** Trapped air in ice cores is fractionated from the contemporary atmosphere by gravitational settling (57, 58), thermal fractionation (59, 60), disequilibrium fractionation due to a convective zone (61), barometric pumping, and net downward advection of air (32, 62). As in Bereiter et al. (20), we corrected the raw elemental ratios with argon isotopes for gravitational settling. The low-accumulation EDC site is subjected to a permanent temperature gradient throughout the firn column, leading to thermal diffusion. This thermal gradient was derived and corrected for based on transient runs of a calibrated 1D ice-flow model connected to a dynamic heat advection and diffusion model (63). The thickness of the diffusive firn column (for the thermal gradient) was diagnosed from the isotopic enrichment, and the resulting firn temperature gradient was scaled to modern firn temperature measurements to calibrate the model. The isotopic data point to the need to include a term representing differential kinetic fractionation in addition to gravitational and thermal fractionation. The possible influence of kinetic fractionation on our results is explored in *SI Appendix*. Corrections for the thermal fractionation scale with surface-temperature change, which are more gradual in Antarctica than in Greenland. Thus, MOTs derived from Antarctic ice cores have smaller uncertainties and are preferred for this application.

**Box Model.** To translate atmospheric  $\delta\text{Xe}/\text{Kr}$ ,  $\delta\text{Xe}/\text{N}_2$ , and  $\delta\text{Kr}/\text{N}_2$  ratios into MOT, we used the four-box model described in Bereiter et al. (19, 20) with the following modifications: No assumptions were made for a possible change in saturation state of the heavy noble gases in the ocean (64, 65) or the potential expansion in the fraction of Antarctic Bottom Water in the deep ocean. The box model produces separate MOTs based on  $\delta\text{Xe}/\text{Kr}$ ,  $\delta\text{Xe}/\text{N}_2$ , and  $\delta\text{Kr}/\text{N}_2$  that should conform within their uncertainties. For EDC, we note a small offset between the three MOT proxies for ice older than 25 ka, which increases with age (*SI Appendix*, Fig. S5). The offset is likely related to gas loss and increasing clathratization with depth into the brittle ice zone. Alternatively, an insufficiently diagnosed fractionation in the firn could explain this offset. However, this would be hard to reconcile with the systematically increasing offset we observed. For our analysis, we used the average of all three individual elemental ratios to reduce the noise from single measurements, but our results are largely unaffected by the somewhat arbitrary choice of MOT proxy. The same conclusions would be reached by looking at  $\delta\text{Kr}/\text{N}_2$ ,  $\delta\text{Xe}/\text{Kr}$ , or  $\delta\text{Xe}/\text{N}_2$  individually. The total uncertainty of the derived MOT for a single sample after correction for firn effects and calibration using the box model is  $\pm 0.4$  K.

**PRI Calculation.** MOT was converted to OHC by multiplying the temperature change with the specific heat of sea water and the mass of the ocean, neglect-

ing the temperature dependence of the specific heat capacity, which is an order of magnitude smaller than other uncertainties in the reconstruction. The ice-sheet contribution was calculated as GMSL equivalent mass change times the specific latent heat of fusion for freshwater. The additional energy required to warm the ice to the freezing point was estimated to be  $\sim 10\%$  of the latent heat (assuming an average ice temperature of  $-20^\circ\text{C}$ ) and was added to the LHM, including a large error reflective of the speculative nature of the average ice-sheet temperature estimate. Changes in the heat content of the atmosphere and the land components were both neglected, as they are at least one order of magnitude smaller than the OHC increase during the current warming period (66, 67). A more thorough assessment of the energy change in different climate system components is presented in *SI Appendix*. The global radiative imbalance PRI is then calculated as  $\text{PRI} = \frac{\partial \Delta E_{\text{tot}}}{\partial t} \times A_{\text{sfc}}^{-1}$ , with  $A_{\text{sfc}}$  being the surface area of Earth.

**Smoothing of the OHC and LHM Records.** Because the radiative imbalance is the derivative of the total energy time series, which includes intrinsic instrumental noise, some smoothing is desirable to get robust results. Low-pass filtering was performed by a smoothing spline (68) with a cutoff period of 2,500 y for the OHC and LHM time series. A sensitivity experiment shows that smoothing with cutoff periods of  $< 2,000$  y leads to large fluctuations of PRI, while very large cutoff periods lower the peaks (*SI Appendix*, Fig. S2).

**Uncertainty Estimation.** Uncertainties were assessed by propagating measurement errors in a Monte Carlo fashion through the entire evaluation routine, including uncertainties in the firn thermal gradient. However, structural systematic uncertainties, such as the setup of the box model, the way the gravitational fractionation is corrected for, or the influence of gas loss on our MOT records, could not be accounted for and are likely larger than the quoted measurement error.

**ACKNOWLEDGMENTS.** We thank Jakob Schwander for EDC firn temperature data; Eric Galbraith and Joel Pedro for helpful discussions on the oceanic heat budget; Christoph Nehrbass-Ahles, Olivier Eicher, and Gregory Teste for sample cutting and transport; and two anonymous reviewers for helpful comments. The research leading to these results was supported by the European Research Council (ERC) under the European Union's Seventh Framework Program FP7/2007-2013 ERC Grant 226172 (ERC Advanced Grant Modern Approaches to Temperature Reconstructions in Polar Ice Cores) and the Swiss National Science Foundation. This work is a contribution to EPICA, a joint European Science Foundation/European Commission scientific program funded by the European Union and national contributions from Belgium, Denmark, France, Germany, Italy, the Netherlands, Norway, Sweden, Switzerland, and the United Kingdom. The main logistic support was provided by Institut Polaire Français–Paule Emile Victor and Programma Nazionale di Ricerche in Antartide at Dome C. This is EPICA publication no. 311.

1. K. von Schuckmann et al., An imperative to monitor Earth's energy imbalance. *Nat. Clim. Change* **6**, 138–144 (2016).
2. N. G. Loeb et al., Observed changes in top-of-the-atmosphere radiation and upper-ocean heating consistent within uncertainty. *Nat. Geosci.* **5**, 110–113 (2012).
3. J. Hansen et al., Earth's energy imbalance: Confirmation and implications. *Science* **308**, 1431–1435 (2005).
4. D. H. Douglass, R. S. Knox, Ocean heat content and Earth's radiation imbalance. *Phys. Lett. A* **373**, 3296–3300 (2009).
5. D. M. Murphy et al., An observationally based energy balance for the Earth since 1950. *J. Geophys. Res. Atmos.* **114**, D17107 (2009).
6. J. Hansen, M. Sato, P. Kharecha, K. von Schuckmann, Earth's energy imbalance and implications. *Atmos. Chem. Phys.* **11**, 13421–13449 (2011).
7. D. Roemmich et al., Unabated planetary warming and its ocean structure since 2006. *Nat. Clim. Change* **5**, 240–245 (2015).
8. J. S. Ellis, T. H. V. Haar, S. Levitus, A. H. Oort, The annual variation in the global heat balance of the Earth. *J. Geophys. Res. Oceans* **83**, 1958–1962 (1978).
9. N. G. Loeb et al., Advances in understanding top-of-atmosphere radiation variability from satellite observations. *Surv. Geophys.* **33**, 359–385 (2012).
10. K. E. Trenberth, J. T. Fasullo, M. A. Balmaseda, Earth's energy imbalance. *J. Clim.* **27**, 3129–3144 (2014).
11. J. D. Shakun et al., Global warming preceded by increasing carbon dioxide concentrations during the last deglaciation. *Nature* **484**, 49–54 (2012).
12. NGRIP Project Members, High-resolution record of Northern Hemisphere climate extending into the last interglacial period. *Nature* **431**, 147–151 (2004).
13. E. D. Galbraith, T. M. Merlis, J. B. Palter, Destabilization of glacial climate by the radiative impact of Atlantic meridional overturning circulation disruptions. *Geophys. Res. Lett.* **43**, 8214–8221 (2016).
14. P. U. Clark et al., Global climate evolution during the last deglaciation. *Proc. Natl. Acad. Sci. U.S.A.* **109**, E1134–E1142 (2012).
15. S. P. Ritz, T. F. Stocker, J. P. Severinghaus, Noble gases as proxies of mean ocean temperature: Sensitivity studies using a climate model of reduced complexity. *Quat. Sci. Rev.* **30**, 3728–3741 (2011).
16. S. Levitus et al., World ocean heat content and thermocline sea level change (0–2000 m), 1955–2010. *Geophys. Res. Lett.* **39**, L10603 (2012).
17. J. A. Church et al., Revisiting the Earth's sea-level and energy budgets from 1961 to 2008. *Geophys. Res. Lett.* **38**, L18601 (2011). Correction in: *Geophys. Res. Lett.* **40**, 4066 (2013).
18. M. A. Healy, J. P. Severinghaus, A method to measure  $\text{Kr}/\text{N}_2$  ratios in air bubbles trapped in ice cores and its application in reconstructing past mean ocean temperature. *J. Geophys. Res. Atmos.* **112**, D19105 (2007).
19. B. Bereiter, K. Kawamura, J. P. Severinghaus, New methods for measuring atmospheric heavy noble gas isotope and elemental ratios in ice core samples. *Rapid Commun. Mass Spectrom.* **32**, 801–814 (2018).
20. B. Bereiter, S. Shackleton, D. Baggenstos, K. Kawamura, J. Severinghaus, Mean global ocean temperatures during the last glacial transition. *Nature* **553**, 39–44 (2018).
21. K. Lambeck, H. Rouby, A. Purcell, Y. Sun, M. Sambridge, Sea level and global ice volumes from the last glacial maximum to the Holocene. *Proc. Natl. Acad. Sci. U.S.A.* **111**, 15296–15303 (2014).
22. P. U. Clark, L. Tarasov, Closing the sea level budget at the last glacial maximum. *Proc. Natl. Acad. Sci. U.S.A.* **111**, 15861–15862 (2014).
23. B. Stenni et al., An oceanic cold reversal during the last deglaciation. *Science* **293**, 2074–2077 (2001).
24. S. O. Rasmussen et al., A new Greenland ice core chronology for the last glacial termination. *J. Geophys. Res. Atmos.* **111**, D06102 (2006).
25. S. A. Marcott, J. D. Shakun, P. U. Clark, A. C. Mix, A reconstruction of regional and global temperature for the past 11,300 years. *Science* **339**, 1198–1201 (2013).
26. Z. Liu et al., The Holocene temperature conundrum. *Proc. Natl. Acad. Sci. U.S.A.* **111**, E3501–E3505 (2014).

27. Y. Zhang, H. Renssen, H. Seppä, P. J. Valdes, Holocene temperature trends in the extra-tropical Northern Hemisphere based on inter-model comparisons. *J. Quat. Sci.* **33**, 464–476 (2018).
28. H. Stommel, Determination of water mass properties of water pumped down from the Ekman layer to the geostrophic flow below. *Proc. Natl. Acad. Sci. U.S.A.* **76**, 3051–3055 (1979).
29. J. F. Adkins, K. McIntyre, D. P. Schrag, The salinity, temperature, and  $\delta^{18}\text{O}$  of the glacial deep ocean. *Science* **298**, 1769–1773 (2002).
30. H. Elderfield *et al.*, Evolution of ocean temperature and ice volume through the Mid-Pleistocene climate transition. *Science* **337**, 704–709 (2012).
31. J. D. Shakun, D. W. Lea, L. E. Lisiecki, M. E. Raymo, An 800-kyr record of global surface ocean  $\delta^{18}\text{O}$  and implications for ice volume-temperature coupling. *Earth Planet Sci. Lett.* **426**, 58–68 (2015).
32. B. Birner, C. Buizert, T. J. W. Wagner, J. P. Severinghaus, The influence of layering and barometric pumping on firn air transport in a 2-D model. *Cryosphere* **12**, 2021–2037 (2018).
33. S. Shackleton *et al.*, Is the noble gas-based rate of ocean warming during the Younger Dryas overestimated? *Geophys. Res. Lett.* **10.1029/2019GL082971** (2019).
34. Intergovernmental Panel on Climate Change. *Climate Change 2013: The Physical Science Basis. Contribution of Working Group I to the Fifth Assessment Report of the Intergovernmental Panel on Climate Change* (Cambridge Univ Press, Cambridge, UK, 2013).
35. S. Manabe, R. T. Wetherald, Thermal equilibrium of the atmosphere with a given distribution of relative humidity. *J. Atmos. Sci.* **24**, 241–259 (1967).
36. D. D. B. Koll, T. W. Cronin, Earth's outgoing longwave radiation linear due to  $\text{H}_2\text{O}$  greenhouse effect. *Proc. Natl. Acad. Sci. U.S.A.* **115**, 10293–10298 (2018).
37. K. Caldeira, N. P. Myhrvold, Projections of the pace of warming following an abrupt increase in atmospheric carbon dioxide concentration. *Environ. Res. Lett.* **8**, 034039 (2013).
38. P. Köhler *et al.*, What caused Earth's temperature variations during the last 800,000 years? Data-based evidence on radiative forcing and constraints on climate sensitivity. *Quat. Sci. Rev.* **29**, 129–145 (2010).
39. A. Berger, M. F. Loutre, Insolation values for the climate of the last 10 million years. *Quat. Sci. Rev.* **10**, 297–317 (1991).
40. S. Arrhenius, On the influence of carbonic acid in the air upon the temperature of the ground. *Lond. Edinb. Dublin Philos. Mag. J. Sci.* **41**, 237–276 (1896).
41. S. A. Marcott *et al.*, Centennial-scale changes in the global carbon cycle during the last deglaciation. *Nature* **514**, 616–619 (2014).
42. R. H. Rhodes *et al.*, Enhanced tropical methane production in response to iceberg discharge in the North Atlantic. *Science* **348**, 1016–1019 (2015).
43. A. Schilt *et al.*, Isotopic constraints on marine and terrestrial  $\text{N}_2\text{O}$  emissions during the last deglaciation. *Nature* **516**, 234–237 (2014).
44. K. E. Kohfeld, Z. Chase, Temporal evolution of mechanisms controlling ocean carbon uptake during the last glacial cycle. *Earth Planet Sci. Lett.* **472**:206–215 (2017).
45. P. Köhler, C. Nehrbass-Ahles, J. Schmitt, T. F. Stocker, H. Fischer, A 156 kyr smoothed history of the atmospheric greenhouse gases  $\text{CO}_2$ ,  $\text{CH}_4$ , and  $\text{N}_2\text{O}$  and their radiative forcing. *Earth Syst. Sci. Data* **9**, 363–387 (2017).
46. A. Abe-Ouchi *et al.*, Ice-sheet configuration in the CMIP5/PMIP3 last glacial maximum experiments. *Geosci. Model Dev.* **8**, 3621–3637 (2015).
47. P. O. Hopcroft, P. J. Valdes, S. Woodward, M. M. Joshi, Last glacial maximum radiative forcing from mineral dust aerosols in an Earth system model. *J. Geophys. Res. Atmos.* **120**, 8186–8205 (2015).
48. S. Albani *et al.*, Paleodust variability since the last glacial maximum and implications for iron inputs to the ocean. *Geophys. Res. Lett.* **43**, 3944–3954 (2016).
49. C. S. Bretherton, Insights into low-latitude cloud feedbacks from high-resolution models. *Philos. Trans. A Math. Phys. Eng. Sci.* **373**, 20140415 (2015).
50. J. B. Pedro *et al.*, Beyond the bipolar seesaw: Toward a process understanding of interhemispheric coupling. *Quat. Sci. Rev.* **192**, 27–46 (2018).
51. J. F. McManus, R. Francois, J. M. Gherardi, L. D. Keigwin, S. Brown-Leger, Collapse and rapid resumption of Atlantic meridional circulation linked to deglacial climate changes. *Nature* **428**, 834–837 (2004).
52. S. P. Ritz, T. F. Stocker, J. O. Grimalt, L. Menviel, A. Timmermann, Estimated strength of the Atlantic overturning circulation during the last deglaciation. *Nat. Geosci.* **6**, 208–212 (2013).
53. J. C. H. Chiang, M. Biasutti, D. S. Battisti, Sensitivity of the Atlantic intertropical convergence zone to last glacial maximum boundary conditions. *Paleoceanography* **18**, 1094 (2003).
54. W. Broecker, A. E. Putnam, How did the hydrologic cycle respond to the two-phase mystery interval? *Quat. Sci. Rev.* **57**, 17–25 (2012).
55. WAIS Divide Project Members, Precise interglacial phasing of abrupt climate change during the last ice age. *Nature* **520**, 661–665 (2015).
56. D. Veres *et al.*, The Antarctic ice core chronology (AICC2012): An optimized multi-parameter and multi-site dating approach for the last 120 thousand years. *Clim. Past* **9**, 1733–1748 (2013).
57. H. Craig, Y. Horibe, T. Sowers, Gravitational separation of gases and isotopes in polar ice caps. *Science* **242**, 1675–1678 (1988).
58. T. Sowers, M. Bender, D. Raynaud, Elemental and isotopic composition of occluded  $\text{O}_2$  and  $\text{N}_2$  in polar ice. *J. Geophys. Res. Atmos.* **94**, 5137–5150 (1989).
59. K. E. Grew, T. L. Ibbs, *Thermal Diffusion in Gases* (Cambridge Univ Press, Cambridge, UK, 1952).
60. J. P. Severinghaus, T. Sowers, E. J. Brook, R. B. Alley, M. L. Bender, Timing of abrupt climate change at the end of the Younger Dryas interval from thermally fractionated gases in polar ice. *Nature* **391**, 141–146 (1998).
61. K. Kawamura *et al.*, Kinetic fractionation of gases by deep air convection in polar firn. *Atmos. Chem. Phys.* **13**, 11141–11155 (2013).
62. C. Buizert, J. P. Severinghaus, Dispersion in deep polar firn driven by synoptic-scale surface pressure variability. *Cryosphere* **10**, 2099–2111 (2016).
63. A. Michel, "Transient modeling of borehole temperature and basal melting in an ice sheet," MSc Thesis, University of Bern, Bern, Switzerland (2016).
64. R. C. Hamme, J. P. Severinghaus, Trace gas disequilibria during deep-water formation. *Deep Sea Res Oceanogr. Res. Pap.* **54**, 939–950 (2007).
65. B. Loose *et al.*, Estimating the recharge properties of the deep ocean using noble gases and helium isotopes. *J. Geophys. Res. Oceans* **121**, 5959–5979 (2016).
66. H. Beltrami, J. E. Smerdon, H. N. Pollack, S. Huang, Continental heat gain in the global climate system. *Geophys. Res. Lett.* **29**, 8-1–8-3 (2002).
67. S. Levitus, J. Antonov, T. Boyer, Warming of the world ocean, 1955–2003. *Geophys. Res. Lett.* **32**, L02604 (2005).
68. I. G. Enting, On the use of smoothing splines to filter  $\text{CO}_2$  data. *J. Geophys. Res. Atmos.* **92**, 10977–10984 (1987).
69. P. Huybers, Early Pleistocene glacial cycles and the integrated summer insolation forcing. *Science* **313**, 508–511 (2006).
70. W. R. Peltier, D. F. Argus, R. Drummond, Space geodesy constrains ice age terminal deglaciation: The global ICE-6G.C (VM5a) model. *J. Geophys. Res. Solid Earth* **120**, 450–487 (2015).